



Ferritin-nanocaged aggregation-induced emission nanoaggregates for NIR-II fluorescence-guided noninvasive, controllable male contraception

Xinghua Yu^{a,*}, Jiaxue Shuai^a, Ge Meng^a, Shumin Zhou^a, Amali Upekshika Wijayaraja^a, Yixiang Zhao^a, Lei Yao^a, Rui Yao^a, Xing Yang^b, Tianfu Zhang^{c,**}, Liying Wang^a, Pengyu Gu^a, Pengfei Zhang^b, Fei Sun^{a,***}

^a Department of Urology & Andrology, Sir Run Run Shaw Hospital, Zhejiang University School of Medicine, Hangzhou, Zhejiang, 310016, China

^b Guangdong Key Laboratory of Nanomedicine, Shenzhen Engineering Laboratory of Nanomedicine and Nanoformulations, CAS-HK Joint Lab for Biomaterials, Shenzhen Institute of Advanced Technology, Chinese Academy of Sciences, Shenzhen, 518055, China

^c School of Biomedical Engineering, Guangzhou Medical University, Guangzhou, 511495, China

ARTICLE INFO

Keywords:

Aggregation-induced emission
Ferritin
Male contraception
Nanoaggregate
Noninvasive

ABSTRACT

Controllable contraception in male animals was demonstrated through the utilization of gold nanorods' photothermal effect to accomplish mild testicular hyperthermia. However, the challenges arising from testicular administration and the non-biodegradability of nanoparticles hinder further clinical implementation. Therefore, a straightforward, non-invasive, and enhanced contraception approach is required. This study explores the utilization of human heavy chain ferritin (HF_n) nanocarriers loaded with aggregation-induced emission luminogens (AIEgens) for noninvasive, controllable male contraception guided by Near-Infrared-II (NIR-II) fluorescence imaging. The HF_n-caged AIEgens (HF_n@BBT) are delivered via intravenous injection and activated by near-infrared irradiation. Lower hyperthermia treatment induces partial damage to the testes and seminiferous tubules, reducing fertility indices by approximately 100% on the 7th day, which gradually recovers to 80% on the 60th day. Conversely, implementation of elevated hyperthermia therapy causes total destruction of both testes and seminiferous tubules, leading to a complete loss of fertility on the 60th day. Additionally, the use of AIEgens in NIR-II imaging offers improved fluorescence efficiency and penetration depth. The findings of this study hold significant promise for the advancement of safe and effective male contraceptive methods, addressing the need for noninvasive and controllable approaches to reproductive health and population control.

1. Introduction

Promoting reproductive health and addressing population control concerns in household pets and livestock farming requires the development of safe, non-invasive, and controlled methods of male contraception [1]. Among the novel methods, the temporary suppression of spermatogenesis and testicular function via the use of mild testicular hyperthermia has displayed potential in attaining reversible male contraception [2,3]. Our research team has made remarkable progress in the area of nanocontraception by studying the direct injection of gold nanorods into the testes and utilizing near-infrared (NIR) irradiation. This study has verified the capability of achieving controlled contraception in males [2]. However, certain clinical applications face

limitations due to issues like pain and damage associated with testicular injection and concerns about potential chronic systemic toxicity from non-degradable thermic agents. Hence, the development of effective, non-invasive, and safe methods for male contraceptive hyperthermia remains a crucial challenge.

Driven by the rapid progress in nanotechnology, nanocarriers have emerged as an incredibly promising strategy for precise drug delivery [4–9]. In particular, human heavy chain ferritin (HF_n) has garnered attention as an effective drug delivery carrier for cancer therapy [10–13]. Through its specific binding to transferrin receptor 1 (TfR1), ferritin can specifically target cancer cells [14–16]. Ferritin, a conserved protein renowned for its iron binding and storage capabilities, possesses a self-assembling structure comprised of a hollow protein shell and this

* Corresponding author.

** Corresponding author.

*** Corresponding author.

E-mail addresses: yuxinghua@zju.edu.cn (X. Yu), zhangtf@gzmu.edu.cn (T. Zhang), sunfeirsh@zju.edu.cn (F. Sun).

shell exhibits an outer diameter measuring 12 nm and an inner diameter measuring 8 nm [11,17–20]. In mammals, the predominant types of ferritin include HFfn and light chain ferritin [21–25]. Among these, HFfn has mainly been employed as a nanocarrier for targeted therapeutic and diagnostic applications in cancer [26,27]. Recent studies have demonstrated the successful inhibition of tumor growth in mouse models through the use of drug-loaded HFfn [28,29]. Significantly, HFfn exhibits the remarkable capability to cross the blood-brain barrier (BBB) and selectively bind to receptors found on glioma cells [30]. Furthermore, the emerging research indicates that HFfn's capability to traverse the blood-testis barrier (BTB) and selectively target elongated sperm cells positions it as a promising candidate for non-invasive and targeted contraception by facilitating the delivery of photothermal agents [31].

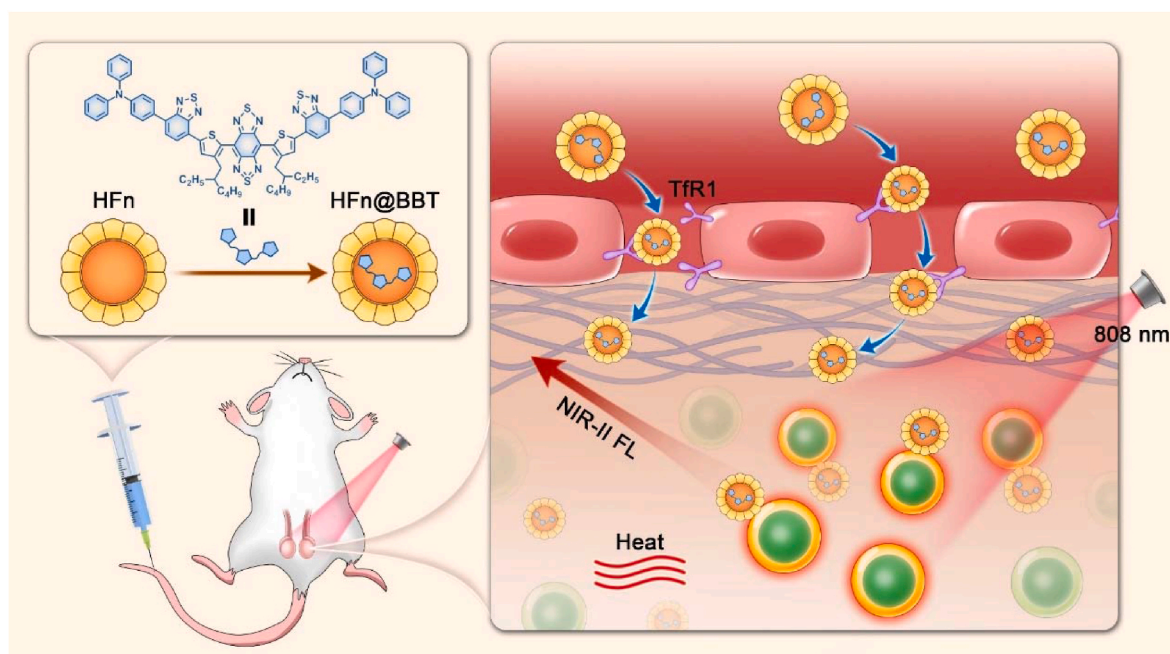
Through mild hyperthermia, the conversion of absorbed light energy into heat by photothermal agents can result in the temporary suppression of spermatogenesis and testicular function. This provides a means for achieving reversible contraception [32]. Aggregation-induced emission luminogens (AIEgens) are a type of photothermal agent that exhibit flexible conformations, facilitating the dispersion of excited-state energy through nonradiative pathways [33–36]. Furthermore, AIEgens have demonstrated an improved ability to perform fluorescence imaging within the range of the NIR-II window (900–1700 nm) in the NIR spectrum [37–39]. NIR-II fluorescence imaging offers numerous benefits, including improved signal-to-background ratios and enhanced depth of penetration. These attributes make it well-suited for *in vivo* bio-imaging purposes [40]. Traditional organic fluorophores used in NIR-II imaging often suffer from aggregation-caused quenching (ACQ), which affects their performance [41–43]. However, AIEgens overcome this limitation by exhibiting strong emission in the aggregated state, leading to improved imaging accuracy and efficiency [44–46].

In this study, we utilized the disassembly and reassembly ability of HFfn under pH control to encapsulate a kind of AIEgens BBTDT-BT-TPA (BBT) within its cavity. By administering HFfn-caged AIEgens (HFfn@BBT) via intravenous injection in male mice and applying NIR irradiation, we successfully induced temporary or permanent male infertility. Under lower hyperthermia treatment, there were partial injuries to the testes and seminiferous tubules, leading to decreased fertility indices of 100% at day 7, which subsequently recovered to 80%

by day 60. Nevertheless, when subjected to more intense hyperthermia treatment, the testes and seminiferous tubules underwent complete destruction, leading to a decline in fertility indices to 0 by day 60. Additionally, the use of AIEgens in NIR-II imaging offers improved fluorescence efficiency and penetration depth. The findings of this study hold significant promise for the advancement of safe and effective male animal contraceptive methods, addressing the need for noninvasive and controllable approaches to reproductive health and animal population control.

2. Results and discussions

HFfn has become increasingly recognized as a highly promising nanocarrier for the purpose of drug delivery, attributed to its stable structure and remarkable targeting capabilities. The synthesis process of HFfn@BBT is presented in Scheme 1. Initially, the structure of BBT was confirmed using ^1H NMR spectra (Fig. S1). Additionally, the energy gaps between LUMO and HOMO for BBT were calculated to be 1.74 eV, indicating strong charge transfer characteristics of fluorophores (Fig. S2). The AIE curve of BBT in Fig. S3 further demonstrated its evident fluorescence intensity increased with increasing water fraction. The UV–Vis curve and fluorescence curve of BBT in Figs. S4 and S5 showed that different solvents had no impact on the absorbance and emission of BBT. Subsequently, utilizing the pH-controlled disassembly and reassembly capability of HFfn, BBT was encapsulated within the HFfn cavity. The morphology of HFfn and HFfn@BBT was illustrated in the TEM images (Fig. 1a–c, and Fig. S6). Statistical TEM analysis (Fig. 1b–d) reveals average lateral sizes of 11.84 ± 0.80 nm and 10.88 ± 0.93 nm, respectively, indicating no significant change in the nanocage structure. Absorption and emission spectra (Fig. 1e and f) exhibit broad bands, peaking at 488 nm and 937 nm, respectively. This fluorescence enhancement is further observed in Fig. 1f after BBT encapsulation. The zeta potential of HFfn@BBT in PBS is -16.03 mV (Fig. 1g), indicating no significant change in charge after encapsulating BBT within the HFfn cavity. Photothermal experiments demonstrate temperature increases to 32.8 °C and 49.3 °C for 10 $\mu\text{g}/\text{mL}$ and 200 $\mu\text{g}/\text{mL}$ HFfn@BBT suspensions, respectively, within 10 min (Fig. 1h). Under the same conditions, the temperatures reached by HFfn@BBT $+1.0$ W/cm 2 and HFfn@BBT



Scheme 1. Schematic representation of ferritin-nanocaged aggregation-induced emission nanoaggregates, that is for NIR-II fluorescence-guided noninvasive, controllable male contraception. Human heavy chain ferritin (HFfn), BBTDT-BT-TPA (BBT), transferrin receptor 1 (TfR1), near-infrared II fluorescence (NIR-II FL).

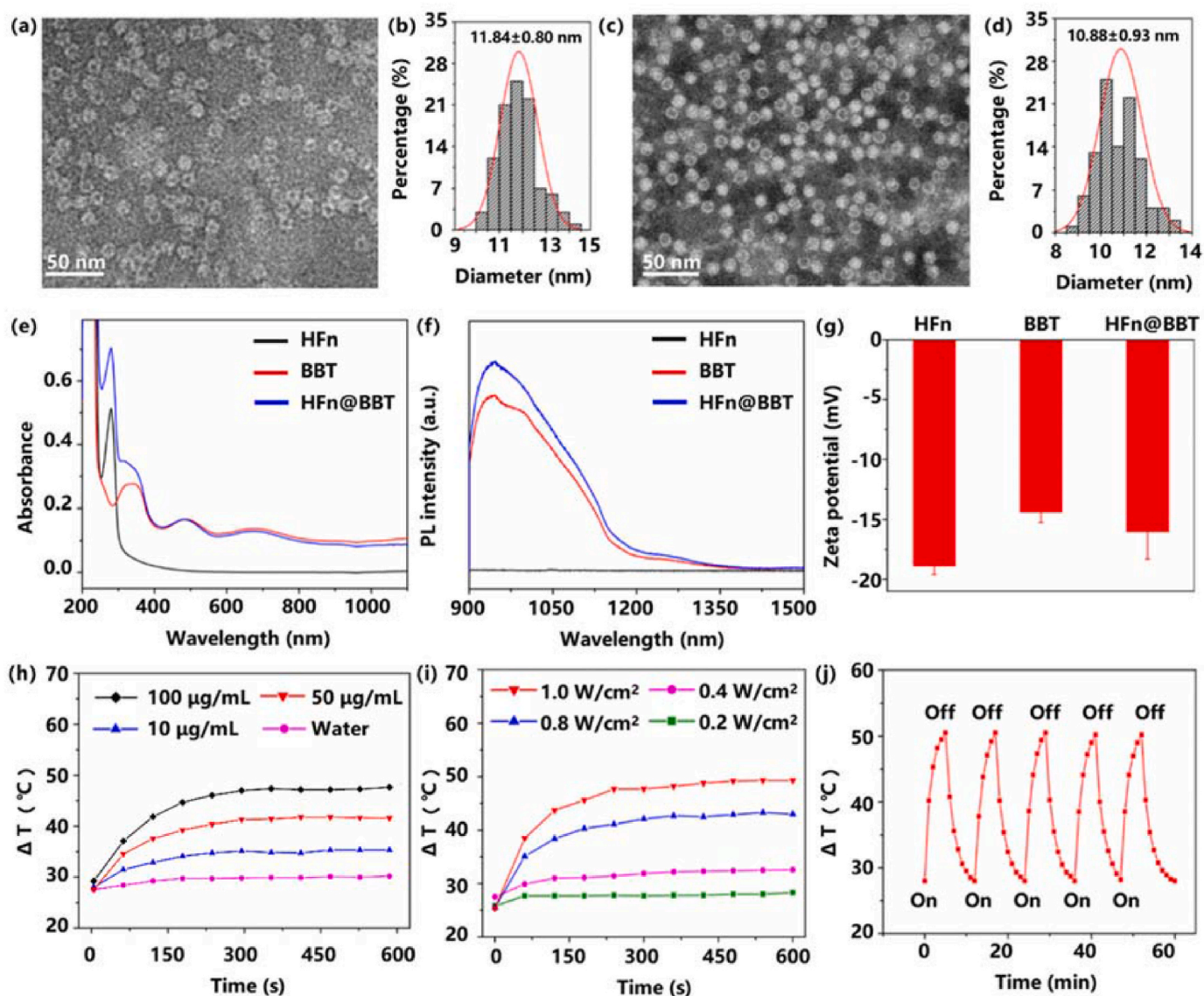


Fig. 1. (a) TEM image of HFfn (scale bar = 50 nm). (b) Statistical analysis of the lateral sizes of HFfn determined by TEM. (c) TEM image of HFfn@BBT (scale bar = 50 nm). (d) Statistical analysis of the lateral sizes of HFfn@BBT determined by TEM. (e) UV-Vis curve of HFfn, BBT and HFfn@BBT. (f) Fluorescence curve of HFfn, BBT and HFfn@BBT. (g) Zeta potential of HFfn, BBT and HFfn@BBT. (h) Photothermal performance of HFfn@BBT solutions at various concentrations. (i) Photothermal performance of HFfn@BBT solutions at different power densities. (j) Photothermal performance of the HFfn@BBT solutions for five laser on/off cycles.

+0.8 W/cm² were 49.3 °C and 43 °C, respectively (Fig. 1i). The photothermal conversion efficiency of BBT and HFfn@BBT was measured at 11.46% and 22.7%, respectively (Fig. S7). Furthermore, following undergoing five cycles of temperature rise and fall, HFfn@BBT displayed consistent photothermal properties (Fig. 1j and Fig. S8), and there was no significant change in the absorption value after storage for one week, highlighting its reliability. These findings suggest that precise temperature control can be achieved by adjusting the concentration of HFfn@BBT or laser intensity.

Following the confirmation of the *in vitro* photothermal performance of HFfn@BBT, the drug delivery capability of HFfn@BBT to male reproductive cells was evaluated. Previous research has demonstrated that HFfn nanocarriers possess the ability to traverse the BTB via the TfR1 in Sertoli cells, facilitating drug delivery to the seminiferous tubules for addressing various diseases [31]. To investigate the ability of HFfn@BBT to pass through the blood-testis barrier (BTB), an *in vitro* model of the BTB was created by growing Sertoli cells in a Transwell plate. Once the Sertoli cells had reached full confluence and established a cellular wall in the culture, FITC-HFfn was introduced into the upper chamber and

incubated for various durations. Subsequently, both of the culture medium in the apical and basal chambers were collected, and the fluorescence signal of FITC-HFfn was measured (Fig. S9A). The signal intensity from the bottom chamber's medium was notably higher than that in the control group, while significantly lower than the top chamber's medium (Fig. S9B). This result indicated the ability of HFfn@BBT to pass through the blood-testis barrier with the assistance of Sertoli cells. Additionally, we investigated the internalization of HFfn@BBT in various types of male reproductive cells, including spermatogonia cells (GC-1 spg), Sertoli cells (TM4), and testicular mesenchymal cells (TM3) [47]. The examination of cellular uptake was conducted using confocal laser scanning microscopy (CLSM). Additionally, the expression of transferrin receptor 1 (TfR1), the native receptor for HFfn, on the cell membranes of TM3, TM4, and GC-1 spg cells, and its interaction with HFfn@BBT, were investigated by immunofluorescence. The immunostaining results (Fig. 2) demonstrated the widespread expression of TfR1 in various cell types, including TM3, TM4, and GC-1 spg cells. The uptake of HFfn@BBT by these cells was observed, and colocalization of FITC-HFfn@BBT and TfR1 indicated their interaction at the cell surface. To further confirm

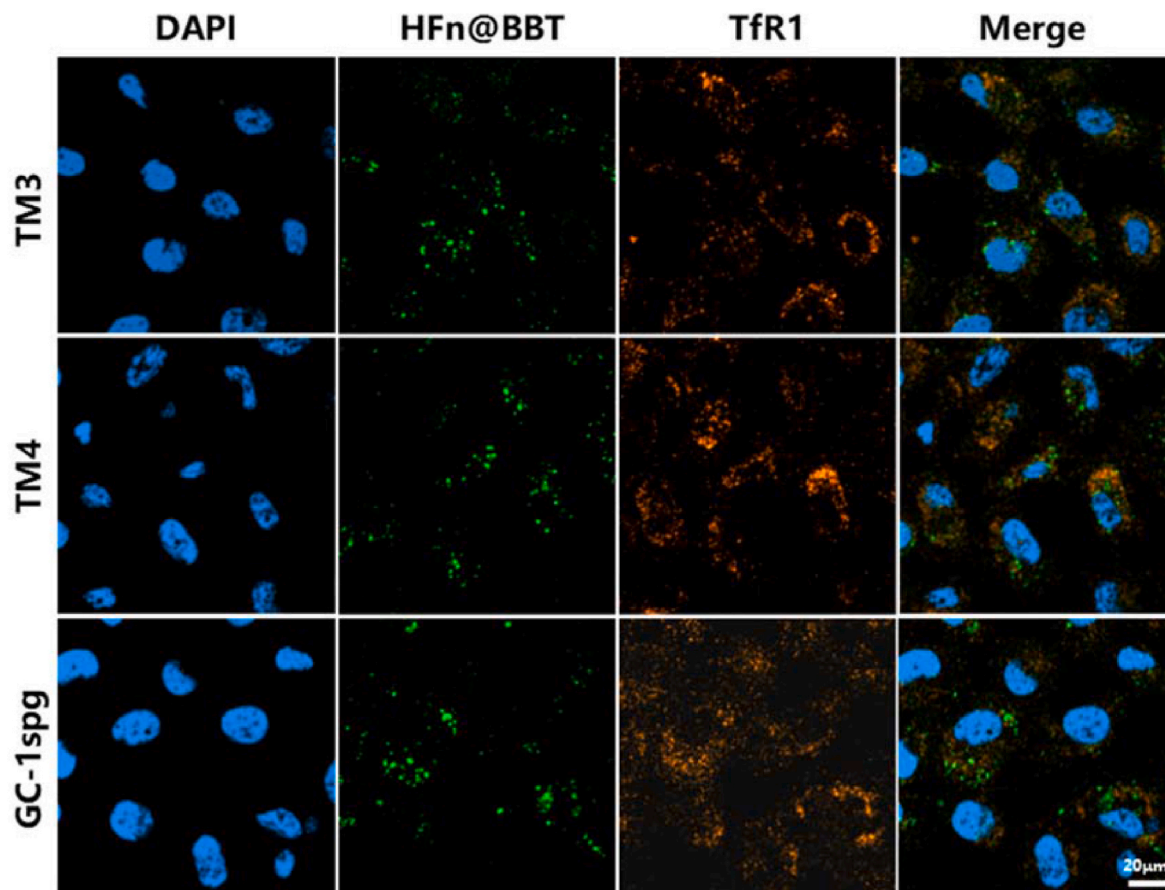


Fig. 2. The cellular uptake of FITC-HFn@BBT in TM3, TM4, and GC-1 spg cells by CLSM imaging. Transferrin receptor 1 (TfR1) monoclonal antibody was utilized, and it was followed by the application of an Alexa Fluor 555 secondary antibody. The excitation wavelength of the fluorescence spectrum includes 405 nm, 488 nm, and 553 nm for DAPI, FITC, and Alexa Fluor 555, respectively. The scale bar in the image represents 20 μm .

the capability to deliver BBT, we incubated two other materials as control groups to validate its delivery ability. The results indicated that HFn exhibited a higher ability to deliver BBT into the cells compared to bovine serum albumin (BSA) and PEG-DSPE (Figs. S10–12), consistent with the cellular uptake of HFn@BBT. To explore the intracellular distribution of HFn@BBT, we examined its localization with several organelles, including the endoplasmic reticulum (ER), lysosome (Lyso), and mitochondria (Mito). As shown in Figs. S13–15, HFn@BBT displayed strong colocalization with ER and Lyso, but weak colocalization with Mito. Additionally, flow cytometer measurements of the cellular uptake of HFn-FITC by GC1-spg cells further validated that HFn effectively delivered functional molecules into the cells (Fig. S16). To explore the impact of temperature on cells, we assessed the viability of GC-1 spg cells cultured at various temperatures for 10 min. At 40 °C, the viability of GC-1 spg cells decreased slightly and recovered after some time, while the viability sharply decreased when cultured at 45 °C and did not recover again, demonstrating that the photothermal effect of HFn@BBT under such conditions is sufficient to kill cells (Fig. S17). Furthermore, to assess the effect of mild hyperthermia treatment, we examined the change in heat shock protein (HSP) levels. In comparison with the PBS group, the expression of HSP70 was notably enhanced when treated with HFn@BBT and NIR laser radiation (Fig. S18), indicating that mild hyperthermia treatment increased the HSP expression.

To explore the potential of the HFn@BBT noninvasive delivery platform in an actual living organism, animal assays were conducted to confirm the promising *in vitro* findings. The biodistribution study utilized an *in vivo* imaging system that harnessed the inherent fluorescence of HFn@BBT. As depicted in Fig. 3a, free injected HFn@BBT mainly accumulated in the liver, with reduced fluorescence observed on the

48th hour. Moreover, HFn@BBT exhibited progressively enhanced fluorescence signals at the testicle site within 24 h post-injection, with a slight decrease on the 48th hour. Therefore, the 24-h time point was selected for laser irradiation. A semi-quantitative approach was employed to quantify the accumulation of HFn@BBT in the testicles by measuring average fluorescence signals. Mice were euthanized at different time intervals (0, 3, 12, 24, and 48 h) subsequent to the injection of HFn@BBT. After excised the testicles, *ex vivo* fluorescence images were obtained and then quantified for an analysis purpose (Fig. 3b, c, and S19). In addition, semi-quantitative biodistribution analysis in Fig. S20 indicated that approximately 3.86% of HFn@BBT could be delivered into the testis. The results, consistent with the *in vivo* imaging, further substantiated the targeted delivery of HFn@BBT to the testicle sites. Subsequently, the *in vivo* photothermal effects of HFn@BBT on testicular heating were investigated. Testes injected with PBS or HFn@BBT were subjected to 808 nm laser irradiation for 10 min. Infrared cameras were employed to measure temperature changes within the testes, with laser intensity controlling the heating extent. The groups were labeled as PBS, PBS +0.8 W/cm², PBS +1.0 W/cm², HFn@BBT, HFn@BBT (40 °C), and HFn@BBT (45 °C). As depicted in Fig. 3d, in both the PBS and HFn groups, the testes maintained a constant average temperature of 30.4 °C. However, in mice treated with PBS +0.8 W/cm², PBS +1.0 W/cm², HFn@BBT (40 °C), and HFn@BBT (45 °C), the temperature of the testes rapidly increased within the first minute and then exhibited slight fluctuations, ultimately reaching 36, 38, 40, and 45 °C, respectively (Fig. 3e). These findings suggest that HFn@BBT possesses precise photothermal effects able to generating heat within the testes. The mice treated were carefully monitored and euthanized at appropriate time points for further research purposes.

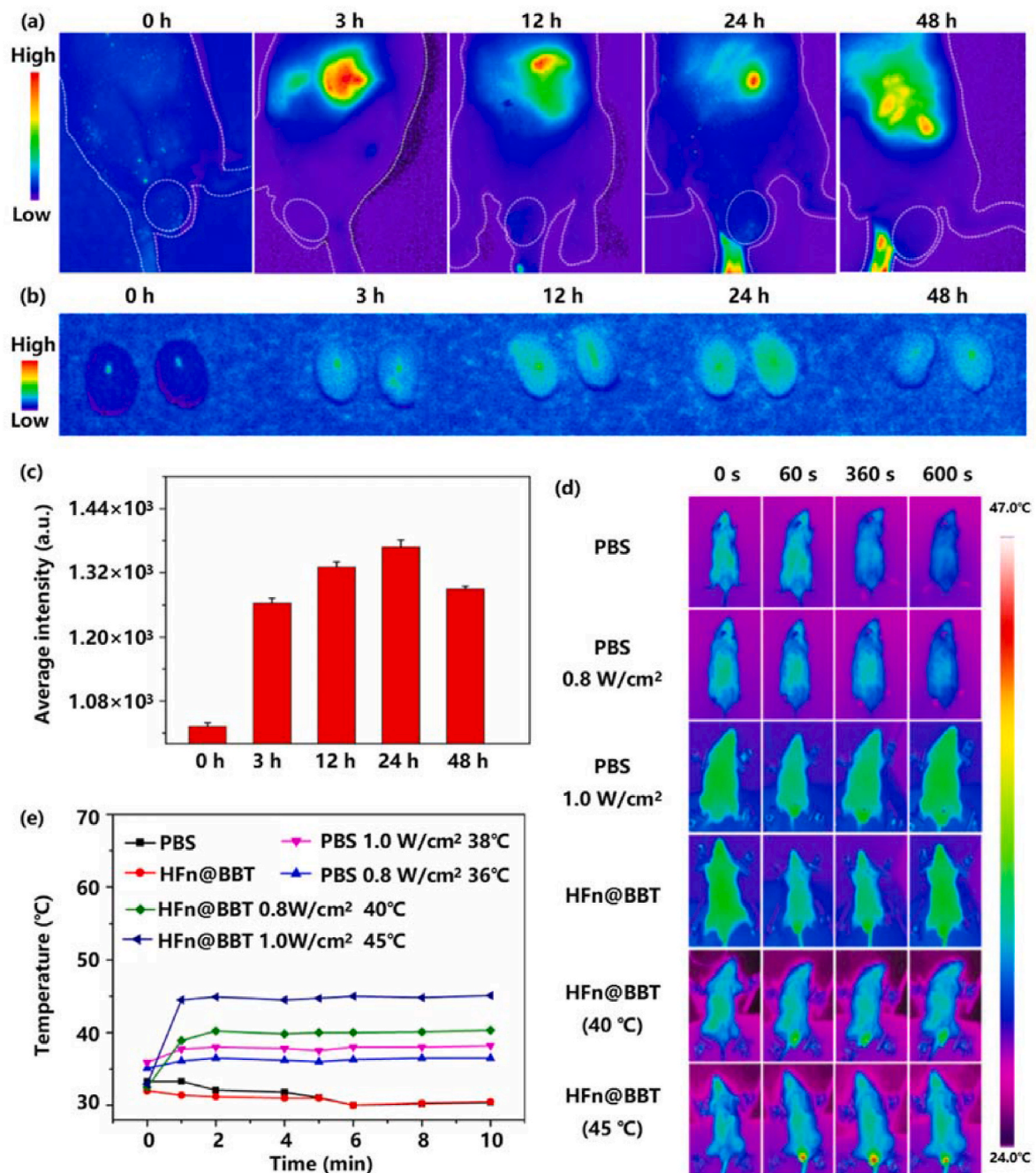


Fig. 3. (a) The mice exhibited noninvasive imaging results using NIR-II fluorescence at different time points after HFn@BBT injection are shown. The testis regions are indicated with a white dotted line. (b) The mice exhibited noninvasive imaging results using NIR-II fluorescence after HFn@BBT injection are shown. HFn@BBT distribution in mice testes at various time points. (c) Semi-quantitative biodistribution analysis of HFn@BBT in experimental mice testes, evaluated based on the average intensity of fluorescence in (b). (d) Images of thermal infrared capturing mouse testes administered with different treatments, subjected to 808 nm laser, captured at various time intervals. (e) Temporal changes in testicular temperature were observed in mice treated with the specified interventions. The experimental mice received intravenous injections of HFn@BBT at a dose of 50 mg/kg.

The contraceptive efficacy of HFn@BBT treatment was evaluated by assessing testicular function, spermatogenesis, and fertility. Four groups were included: PBS, HFn@BBT, HFn@BBT (40 °C), and HFn@BBT (45 °C). The euthanized mice that received treatment were analyzed by dissecting and weighing their testes and epididymides at 7, 30, and 60 days. As expected, at 7 days post-treatment, the testes in the HFn@BBT (40 °C) and HFn@BBT (45 °C) groups exhibited shrinkage and lower weight compared to the PBS and HFn groups, indicating partial destruction (Fig. 4a and Fig. S21). In the epididymis index, no notable variation was detected across the different groups, as depicted in

Fig. S21. In the seminiferous tubules of the HFn@BBT (40 °C) group at 7 days, histological analysis revealed degeneration of spermatocytes and spermatozoa. At 30 and 60 days, the observations demonstrated gradual restoration of spermatogenesis, suggesting reversible inhibition of spermatogenesis. In contrast, the HFn@BBT (45 °C) group showed continued degeneration at 30 and 60 days, indicating irreversible inhibition (Fig. 4b). The histological evaluation of the epididymis at 7 days following treatment with HFn@BBT (40 °C) demonstrated the absence of sperm. However, at 60 days, the presence of sperm was observed, as illustrated in Fig. 4c. At 7 days post-treatment with HFn@BBT (40 °C),

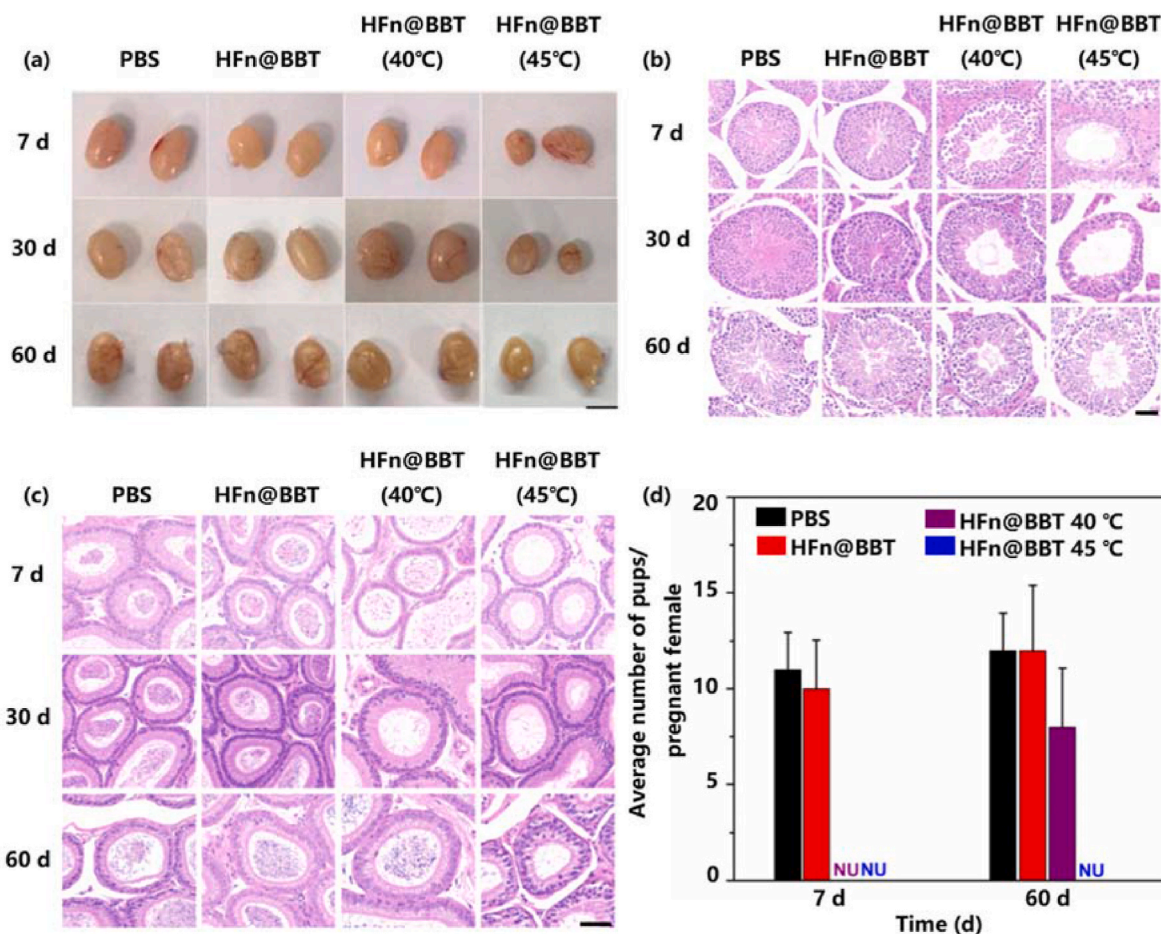


Fig. 4. (a) Testes images captured at 7, 30, and 60 days, with a scale of 5.0 mm. (b) Cross-sections of testicular tissue stained with H&E on the 7th, 30th, 60th day, the scale is 50 μ m. (c) Cross-sections of epididymis stained with H&E at 7, 30, and 60 days, with a scale of 50 μ m. (d) Every average pup count per pregnant female was calculated at 7 and 60 days after treatment, with a total of 5 samples. "NU" denotes none.

fertility indices dropped to 0, but gradually recovered to approximately 80% after 60 days, as depicted in Fig. 4d and Fig. S22. Importantly, no meaningful distinction was noticed in the fertility index between the HFfn@BBT (40 °C) group and the control group, as shown in Fig. S22. Furthermore, no morphological abnormalities were detected in the offspring, and the number of pups in each group was similar. These results demonstrate that HFfn@BBT (40 °C) treatment caused reversible testicular destruction and temporary inhibition of spermatogenesis, resulting in reversible male contraception.

After demonstrating the promising noninvasive and controllable male contraception effects of HFfn@BBT, it was crucial to assess their toxicity. Initially, the cytotoxicity was evaluated in TM3, TM4, and GC-1spg cells using a CCK-8 assay (Fig. S23). As anticipated, HFfn@BBT exhibited minimal cytotoxicity even at a higher concentration of 100 mg/L following 24 h of co-cultivation with TM3, TM4, and GC-1 spg cells, suggesting outstanding biocompatibility. *In vivo* evaluation of systemic toxicity was conducted. The exceptional biosafety of HFfn@BBT was further corroborated by the H&E staining images of vital organs, as illustrated in Fig. S24. Additionally, blood routine tests revealed no significant toxicity, as all data from the treatments stayed within the normal limits, as shown in Fig. S25. Blood biochemical indicators also demonstrated no significant kidney and liver toxicity (Figs. S26–27). Furthermore, throughout the duration of the experiment, no abnormal or stressful behaviors were observed during daily monitoring of the mice. No noticeable disparities in body weight were detected during the entire duration of the study, as illustrated in Fig. S28. To study the removal time of nanoparticles, we studied the amount of the

nanoparticles in the plasma at different time points. According to Fig. S29, it takes approximately 60 h for the nanoparticles to be completely eliminated from the body after intravenous injection. In summary, the ferritin-nanocaged aggregation-induced emission nano aggregates for noninvasive guidance using NIR-II fluorescence and controllable strategy not only demonstrated excellent male contraception effects but also exhibited negligible toxicity.

3. Conclusion

In summary, this study demonstrates the potential of utilizing human heavy chain ferritin (HFfn) nanocarriers loaded with aggregation-induced emission luminogens (AIEgens) for noninvasive and controllable male contraception guided by NIR-II fluorescence imaging. By delivering HFfn-caged AIEgens (HFfn@BBT) intravenously and activating them with NIR irradiation, this study achieves targeted contraception. Mild hyperthermia treatment leads to partial injuries to the testes and seminiferous tubules, resulting in decreased fertility indices of 0% on the 7th day that recover to 80% on the 60th day. Furthermore, the use of AIEgens in NIR-II imaging enhances fluorescence efficiency and accuracy. These findings hold promise for the development of safe and effective male contraceptive methods, addressing the need for noninvasive and controllable approaches to reproductive health and population control in animal populations. Further research and development in this field have the potential to make significant contributions to male contraception, as well as support broader objectives related to reproductive health and population control initiatives.

CRedit authorship contribution statement

Xinghua Yu: Writing – review & editing, Writing – original draft, Visualization, Funding acquisition, Data curation, Conceptualization. **Jiaxue Shuai:** Data curation. **Ge Meng:** Data curation. **Shumin Zhou:** Data curation. **Amali Upekshika Wijayaraja:** Data curation. **Yixiang Zhao:** Data curation. **Lei Yao:** Data curation. **Rui Yao:** Data curation. **Xing Yang:** Formal analysis. **Tianfu Zhang:** Formal analysis. **Liyang Wang:** Formal analysis. **Pengyu Gu:** Data curation. **Pengfei Zhang:** Visualization. **Fei Sun:** Writing – review & editing, Funding acquisition, Conceptualization.

Declaration of competing interest

The authors declare that they have no known competing financial interests or personal relationships that could have appeared to influence the work reported in this paper.

Data availability

Data will be made available on request.

Acknowledgements

(The National Natural Science Foundation of China (No. 82371613 to F.S); The National Key Research and Development Program of China (No. 2021YFC2700200 to F.S); The Key Research and Development Program of Zhejiang Province (No. 2023C03035 to F.S); The Key Research and Development Program of Ningxia Hui Autonomous Region (No. 2021BEG02029 to F.S); the 2024 Zhejiang Medicine and Health Technology Plan (2024KY100 to X. Y); the 2024 Zhejiang Traditional Chinese Medicine Science and Technology Plan (2024ZL597 to X. Y); the 2024 Zhejiang Basic Public Welfare Research Plan (Q24H180009 to X. Y); the 2023 Clinical Medical Research Special Key Project Fund of the Zhejiang Medical Association (2023ZYC-Z05 to X. Y))

Received: ((will be filled in by the editorial staff)) Revised: ((will be filled in by the editorial staff)) Published online: ((will be filled in by the editorial staff))

Appendix A. Supplementary data

Supplementary data to this article can be found online at <https://doi.org/10.1016/j.mtbio.2024.100995>.

This study explores the utilization of ferritin-nanocaged aggregation-induced emission nanoaggregates for NIR-II fluorescence-guided noninvasive, controllable male contraception. It investigates the potential of human heavy chain ferritin (HFn) as a nanocarrier for targeted testicular delivery. The study aims to achieve reversible male contraception using mild testicular hyperthermia and NIR-II imaging guidance. The findings contribute to the development of effective and noninvasive methods for male contraception.

References

- C.S. Asa, Vet. Clin. Small Anim. Pract. 48 (4) (2018) 733.
- W. Li, C. Sun, F. Wang, Y. Wang, Y. Zhai, M. Liang, W. Liu, Z. Liu, J. Wang, F. Sun, Nano Lett. 13 (6) (2013) 2477.
- C. Paul, A.A. Murray, N. Spears, P.T.K. Saunders, Reproduction 136 (1) (2008) 73.
- G. Xu, X. Yu, J. Zhang, Y. Sheng, G. Liu, W. Tao, L. Mei, Int. J. Nanomed. 11 (2016) 2953.
- W. Liu, X. Wang, X. Gao, X. Chen, X. Yu, H. Wang, X. Deng, Ceram. Int. 39 (7) (2013) 8521.
- X. Yu, M. Lyu, X. Ou, W. Liu, X. Yang, X. Ma, T. Zhang, L. Wang, Y.-C. Zhang, S. Chen, R.T.K. Kwok, Z. Zheng, H.-L. Cui, L. Cai, P. Zhang, B.Z. Tang, Adv. Healthcare Mater. (2023) e2202907.
- W. Tao, X. Zhu, X. Yu, X. Zeng, Q. Xiao, X. Zhang, X. Ji, X. Wang, J. Shi, H. Zhang, L. Mei, Adv. Mater. 29 (1) (2017) 1.
- W. Tao, X. Zeng, J. Wu, X. Zhu, X. Yu, X. Zhang, J. Zhang, G. Liu, L. Mei, Theranostics 6 (4) (2016) 470.
- X. Yu, Y.-C. Zhang, X. Yang, Z. Huang, T. Zhang, L. Yang, W. Meng, X. Liu, P. Gong, A. Forni, Z. Zheng, B. Liu, P. Zhang, L. Cai, B.Z. Tang, Nano Today 44 (2022) 101477.
- M. Liang, K. Fan, M. Zhou, D. Duan, J. Zheng, D. Yang, J. Feng, X. Yan, P Natl Acad Sci USA 111 (41) (2014) 14900.
- Z. Wang, Y. Zhao, S. Zhang, X. Chen, G. Sun, B. Zhang, B. Jiang, Y. Yang, X. Yan, K. Fan, Theranostics 12 (4) (2022) 1800.
- B. Jiang, X. Jia, T. Ji, M. Zhou, J. He, K. Wang, J. Tian, X. Yan, K. Fan, Sci. China Life Sci. 65 (2) (2022) 328.
- X. Cheng, K. Fan, L. Wang, X. Ying, A.J. Sanders, T. Guo, X. Xing, M. Zhou, H. Du, Y. Hu, H. Ding, Z. Li, X. Wen, W. Jiang, X. Yan, J. Ji, Cell Death Dis. 13 (11) (2022) 92.
- K. Fan, C. Cao, Y. Pan, D. Lu, D. Yang, J. Feng, L. Song, M. Liang, X. Yan, Nat. Nanotechnol. 7 (7) (2012) 459.
- J. Li, Z. Zhang, B. Zhang, X. Yan, K. Fan, Biomater Sci-Uk 11 (10) (2023) 3394.
- K. Fan, L. Gao, H. Wei, B. Jiang, D. Wang, R. Zhang, J. He, X. Meng, Z. Wang, H. Fan, T. Wen, D. Duan, L. Chen, W. Jiang, Y. Lu, B. Jiang, Y. Wei, W. Li, Y. Yuan, H. Dong, L. Zhang, C. Hong, Z. Zhang, M. Cheng, X. Geng, T. Hou, Y. Hou, J. Li, G. Tang, Y. Zhao, H. Zhao, S. Zhang, J. Xie, Z. Zhou, J. Ren, X. Huang, X. Gao, M. Liang, Y. Zhang, H. Xu, X. Qu, X. Yan, Progress in Chemistry 35 (1) (2023) 1.
- P.M. Harrison, P. Arosio, Biochim. Biophys. Acta Bioenerg. 1275 (3) (1996) 161.
- Y. Chen, L. Zeng, H. Zhu, Q. Wu, R. Liu, Q. Liang, B. Chen, H. Dai, K. Tang, C. Liao, Y. Huang, X. Yan, K. Fan, J.-Z. Du, R. Lin, J. Wang, Small Methods (2022) e2202907.
- B. Zhang, G. Tang, J. He, X. Yan, K. Fan, Adv. Drug Deliv. Rev. 176 (2021) 113892.
- B. Jiang, X. Chen, G. Sun, X. Chen, Y. Yin, Y. Jin, Q. Mi, L. Ma, Y. Yang, X. Yan, K. Fan, Nano Today 35 (2020) 1800.
- P. Arosio, R. Ingrassia, P. Cavadini, Biochim. Biophys. Acta Gen. Subj. 1790 (7) (2009) 589.
- Y. Zhao, M. Liang, X. Li, K. Fan, J. Xiao, Y. Li, H. Shi, F. Wang, H.S. Choi, D. Cheng, X. Yan, ACS Nano 10 (4) (2016) 4184.
- M. Liang, H. Tan, J. Zhou, T. Wang, D. Duan, K. Fan, J. He, D. Cheng, H. Shi, H. S. Choi, X. Yan, ACS Nano 12 (9) (2018) 9300.
- B. Jiang, R. Zhang, J. Zhang, Y. Hou, X. Chen, M. Zhou, X. Tian, C. Hao, K. Fan, X. Yan, Theranostics 9 (8) (2019) 2167.
- T. Wang, J. He, D. Duan, B. Jiang, P. Wang, K. Fan, M. Liang, X. Yan, Nano Res. 12 (4) (2019) 863.
- Z. Zhen, W. Tang, H. Chen, X. Lin, T. Todd, G. Wang, T. Cowger, X. Chen, J. Xie, ACS Nano 7 (6) (2013) 4830.
- B. Zhang, X. Chen, G. Tang, R. Zhang, J. Li, G. Sun, X. Yan, K. Fan, Nano Today 46 (2022) 101564.
- Z. Yang, X. Wang, H. Diao, J. Zhang, H. Li, H. Sun, Z. Guo, Chem. Commun. 33 (2007) 3453.
- Z. Zhen, W. Tang, C. Guo, H. Chen, X. Lin, G. Liu, B. Fei, X. Chen, B. Xu, J. Xie, ACS Nano 7 (8) (2013) 6988.
- K. Fan, X. Jia, M. Zhou, K. Wang, J. Conde, J. He, J. Tian, X. Yan, ACS Nano 12 (5) (2018) 4105.
- J. Pang, X. Feng, Q. Liang, X.Y. Zheng, Y.M. Duan, X. Zhang, J.B. Zhang, Y. Chen, K.L. Fan, L.Z. Gao, J.X. Li, ACS Nano 16 (3) (2022) 4175.
- X. Yu, X. Cai, H. Cui, S.-W. Lee, X.-F. Yu, B. Liu, Nanoscale 9 (45) (2017) 17859.
- T. Zhang, X. Yang, X. Ou, M.M.S. Lee, J. Zhang, C. Xu, X. Yu, P. Gong, J.W.Y. Lam, P. Zhang, B.Z. Tang, Adv. Mater. (2023) e2303186.
- X. Xu, G. Deng, Z. Sun, Y. Luo, J. Liu, X. Yu, Y. Zhao, P. Gong, G. Liu, P. Zhang, F. Pan, L. Cai, B.Z. Tang, Adv. Mater. 33 (33) (2021) e2102322.
- J. Qi, H.L. Ou, Q. Liu, D. Ding, Aggregate 2 (1) (2021) 95.
- M. Kang, Z. Zhang, N. Song, M. Li, P. Sun, X. Chen, D. Wang, B.Z. Tang, Aggregate 1 (1) (2020) 80.
- X. Yang, T. Yang, Q. Liu, X. Zhang, X. Yu, R.T.K. Kwok, L. Hai, P. Zhang, B.Z. Tang, L. Cai, P. Gong, Adv. Funct. Mater. 32 (45) (2022) 2206346.
- H. Cao, Y. Yang, J. Li, Aggregate 1 (1) (2020) 69.
- S. Cao, J. Shao, L.K.E.A. Abdelmohsen, J.C.M. van Hest, Aggregate 3 (1) (2022) 683.
- Y. Liu, W. Zhen, Y. Wang, J. Liu, L. Jin, T. Zhang, S. Zhang, Y. Zhao, S. Song, C. Li, J. Zhu, Y. Yang, H. Zhang, Angew Chem. Int. Ed. Engl. 58 (8) (2019) 2407.
- Y. Li, S. Liu, H. Ni, H. Zhang, H. Zhang, C. Chuah, C. Ma, K.S. Wong, J.W.Y. Lam, R. T.K. Kwok, J. Qian, X. Lu, B.Z. Tang, Angew Chem. Int. Ed. Engl. 59 (31) (2020) 12822.
- Z. Zhao, Z. Wang, J. Tavakoli, G. Shan, J. Zhang, C. Peng, Y. Xiong, X. Zhang, T. S. Cheung, Y. Tang, B. Huang, Z. Yu, J.W.Y. Lam, B.Z. Tang, Aggregate 2 (2) (2021) 19.
- L. Xu, X. Jiang, K. Liang, M. Gao, B. Kong, Aggregate 3 (1) (2022) 121.
- W. Xu, M.M.S. Lee, J.J. Nie, Z. Zhang, R.T.K. Kwok, J.W.Y. Lam, F.J. Xu, D. Wang, B.Z. Tang, Angew Chem. Int. Ed. Engl. 59 (24) (2020) 9610.
- J. Heo, D.P. Murale, H.Y. Yoon, V. Arun, S. Choi, E. Kim, J.-S. Lee, S. Kim, Aggregate 3 (2) (2022) e159.
- C. Ji, L. Lai, P. Li, Z. Wu, W. Cheng, M. Yin, Aggregate 2 (4) (2021) e39.
- W.H. Ding, Z.C.A. Chen, Y.Y. Gu, Z.R. Chen, Y.Q. Zheng, F. Sun, Nano Lett. 21 (2021) 6289.